Electr Eng (2018) 100:1305–1315
https://doi.org/10.1007/s00202-017-0584-5

ORIGINAL PAPER

Electrical properties and aquatic ecotoxicity effects of ZnS nanocrystals

Anis Fkiri[1] · Nesrine Ben Saber[2] · Badreddine Sellami[3] · Aymen Selmi[4] · Tariq Altalhi[2] · Adil A. Gobouri[2] · Ali Aldalbahi[5] · Amine Mezni[1,2]

Received: 28 February 2017 / Accepted: 12 June 2017 / Published online: 22 June 2017

Abstract A new synthesis method of ZnS colloidal nanocrystals is presented in this work, and this novel approach allows one to produce Zinc sulfide nanocrystals owing to a modified polyol process that makes use of 1.3-propanediol as a solvent. The structure and morphology of the nanoparticles were characterized by high-resolution transmission electron microscopy, transmission electron microscopy, X-ray diffraction and spectroscopy photoluminescence. The results showed that quasi-spherical ZnS nanocrystals with sizes in the range 3–5 nm were formed. Their morphology, size and colloidal stability are driven by the polyol solvent. Under UV excitation, a strong visible PL emission, due to the radiative recombinations of the electron–hole pairs photo-generated in the ZnS nanoparticles, was observed. In order to study the environmental risk of ZnS, mussels *Mytilus galloprovincialis* were exposed to ZnS C1 = 0.1 mg/L, ZnS C2 = 1 mg/L and ZnS C3 = 10 mg/L. Superoxide dismutase, catalase activities and protein thiols density were determined in the gill of treated and untreated mussels. No significant effects were detected in the gills of exposed mussels after 14 days of exposure compared to control. Optical property of the new nanomaterial, together with the easy synthesis process, makes the ZnS nanocrystals a promising candidate for applications optoelectronics and photocatalyst. The frequency-dependent impedance and AC conductivity have been investigated in this context. Impedance and modulus plane plots from 10 to 10^7 Hz show the presence of bulk and grain boundary phases in ZnS at each measurement temperature from 125 to 225 °C. The activation energy was calculated from the temperature variation of DC conductivity. Studies of frequency and temperature dependence of electrical data of the compound suggest that conduction process in the material is thermally activated. Environmental risk assessment results constitute a scientific support for considering the use of this nonmaterial on various applications after further complementary studies in order to ensure the safety of these NPs.

Keywords Zinc sulfide · Polyol medium · 1.3-propanediol · Electrical properties · Aquatic ecotoxicity

✉ Amine Mezni
aminemezni@yahoo.fr

1 Unité de Recherche Synthèse et Structure de Nanomatériaux UR11ES30, Faculté des Sciences de Bizerte, Université de Carthage, 7021 Jarzouna, Bizerte, Tunisia

2 Department of Chemistry, Faculty of Science, Taif University, Taif, Saudi Arabia

3 Institut National des Sciences et Technologies de la Mer, Tabarka, Tunisia

4 Laboratory of Materials, Organization and Properties LabMOP, 2092 El Manar, Tunis, Tunisia

5 Department of Chemistry, College of Science, King Saud University, P.O. Box 2455, Riyadh 11451, Saudi Arabia

1 Introduction

Semiconductor quantum dots have attracted increasing attentions in many fields such as solar cells, optoelectronic transistor component and fluorescent biological tables because of their unique size-dependent electronic and optical properties [1]. Therefore, a variety of semiconductor nanoparticles, such a CdS [2–4], CdSe [5,6], CdTe [7], ZnO [8,9] and ZnS [10,11], have been synthesized during the past decade. Among them, zinc sulfide (ZnS) is a II–VI compound semiconductor with a large direct band gap of about 3.68 eV and a large exciton binding energy (40 meV) at room temperature, as well as absorption coefficient, making it an

ideal candidate for tunable photosensitization and considerable photoactivity in the visible region [12,13]. The fast development of nanoscience and nanotechnology makes ZnS nanomaterials successfully synthesized into diverse morphologies, such as nanorods [14,15], nanowires [16,17], nanoparticles [18], nanocages [19] and nanobelts [20,21]. Since the size and the shape of the semiconductor nanoparticles can control their physical and chemical characters, different methods are developed to get uniform nanoparticles, including solvothermal method synthesis [22,23], hydrothermal synthesis [24,25], vapor deposition process [26], homogeneous precipitation [27], sol–gel method [28] and polyol method [29]. According to the literature, ZnS NPs were synthesized by forced hydrolysis in different polyols solvent such as diethylene glycol (DEG), ethylene glycol (EG) and polyethylene glycol (PEG). Polyol solvent acts as a complexing agent at a time and a surfactant which adsorbs on the surface of the nanoparticles, thereby preventing agglomeration of the nanoparticles. C. Feldmann [30] is among the first who synthesized ZnS nanoparticles by using polyol method as precursors of zinc acetate dihydrate and thiourea dissolved in DEG (diethylene glycol). The solution is rapidly heated to 190 °C and kept at this temperature for 2 hours. Chong et al Bi [31] succeed to synthesize nanoparticles of ZnS with spherical forms using as precursor zinc acetate dihydrate [$Zn(CH_3COO)_2 \cdot 2H_2O$], thiourea ($N_2H_4CS$) and carboxylate polystyrene ($PS\text{-}CO_2$) in ethylene glycol (EG) at a temperature $T = 150\,°C$ for 2h. After their use cycle, nanoparticles enter the environment via different exposure routes, including solid and liquid waste from domestic sources and industrial activity. Several studies have modeled the potential release of NPs into the environment and shown that NPs are expected to be found in the different environmental compartments [32]. In fact, rigorous identification of environmental hazard and full-risk assessments of ZnS nanoparticles are needed. The mussels *Mytilus galloprovincialis* are a natural filter feeding bivalves widely used in biomonitoring system [33,34]. This coastal organism has been used as sentinel species to evaluate the levels of environmental contaminant elements in different ecosystems [35,36]. Quantum dots such as ZnS may affect biochemical processes in living organisms by producing reactive oxygen species (ROS) such as superoxide anion and hydrogen peroxide (Geret et al. 2002; Bebianno and Serafim 2003) influencing their populations. This imposes the need for providing early-warning signals of pollution [37]. The early biochemical responses occurred before other disturbance as population changes, or mortality occur, are measurable endpoints, commonly called biomarkers [38]. Biomarkers such as SOD and CAT represent a changes occurring at biochemical levels, which can be measured in cells or organs within an organism and that may be indicative of xenobiotic exposure and/or effect [39,40]. Superoxide dismutase (SOD) and catalase (CAT) represent a key antioxidant enzymes that neutralize ROS effects. In addition, protein targets of oxidative stress directly absorb 78% of ROS, leading to their potential covalent modification. In bivalves, thiols groups have widely been applied as novel biomarkers of oxidative stress due to environmental stressors [41–43]. In this work, we report in the facile one-pot synthesis of ZnS nanocrystals formed in 1.3-propanediol by using zinc (II) and sulfide (II) precursors. The zinc sulfide nanoparticle was prepared without the addition of any other reagents, template or complex metal ligand. The polyol solvent plays the role of a complexant, a surfactant and a stabilizing agent. On the other hand, owing to their unique structure, the as-prepared have been tested of electrical properties. Additionally, this article describes several approaches that have been developed to assess the environmental risk of ZnS nanoparticles.

2 Experimental procedure

2.1 Synthesis of ZnS nanoparticles

To synthesize the ZnS CNCs, zinc acetate dehydrate [$Zn(OAc)_2 \cdot 2H_2O$) Aldrich, AR grade] (1.15 g) and the thiourea [Sigma-Aldrich] (0.47 g) were dissolved in 25 ml of 1.3-propanediol and the heated at 190 °C and kept at this temperature for 2h under continuous magnetically agitation. At the end of the reaction, the precipitate was centrifuged, washed several times with ethanol and then dried in vacuum at 60 °C for 12 h to yield a white dry ZnS powder.

2.2 Characterization of ZnS nanoparticles

The crystalline structure of the as-prepared powder was characterized by X-ray diffraction (XRD) (an INEL diffractometer with a copper anticathode ($\lambda = 1.54060$ Å)). High-resolution TEM (Philips Tecnai F-20 SACTEM operating at 200 Kv) images provide further insight into the structural information of the ZnS NPs. The optical absorption spectra of ZnS nanoparticles dispersed in ethanol were performed on a PerkinElmer Lambda 11 UV/VIS spectrophotometer. The photoluminescence (PL) measurement was carried out at room temperature using a PerkinElmer MPF-44B spectrophotometer. The excitation source was a monochromator set at 280 nm and illuminated with a xenon XBU-150 lamp. For electrical impedance characterization, the resultant annealed powder material was compacted into disk-shaped pellets of dimension 13 mm in diameter and 1.5 $\pm$ 0.15 mm thickness with 5-thon hydraulic pressure. The dimension of the pellets was measured using an impedance

analyzer (TEGAL 6192 ALF model). To obtain good ohmic contact, silver paint was employed on both sides of the pellets.

2.3 Ecotoxicity determination

Mediterranean mussels *M. galloprovincialis* of both sexes were sampled from Menzel Jemil in Bizerte lagoon (Tunisia) and had a mean size of 5.86 cm. Mussels were collected (depth between 3 and 5 m) from the ropes where they are cultivated in aquaculture farms located in the chosen sites. Mussels were acclimated to laboratory conditions for one week prior to experiments. Exposure was made in 3-L glass tanks with 10 mussels per tank, at constant temperature (19 °C), in darkness, using 1-mm filtered UV-irradiated seawater with oceanic characteristics. Exposure tanks were continuously aerated with 0.22-mm filtered air and were allowed to equilibrate for 1 h, before introducing the mussels. Water was renewed three times per week after feeding mussels for 1 h with a mixed diet of Isochrysis galbana and Tetraselmis suecica. Every day with no water renewal toxicant was added to maintain nominal concentrations assuming an exponential decay. A primary stock solution of ZnS was prepared in the distilled water to a nominal concentration of 10 $g\,L^{-1}$. Fresh stock solutions were prepared every 7 days and stored at 4 °C. To study the concentration–response relationship between ZnS exposure and the biochemical responses, over 120 mussels were exposed for 14 days to experimental solutions containing 0.1, 1 and 10 mg/L of ZnS. After 14-d exposure, samples were taken for biochemical analyses.

Thirty individuals from each experimental group including control group were taken at the end of experiment. Gill of mussels were dissected out and homogenized by a polytron homogenizer in 10 mM Tris/HCl, pH 7.2, containing 500 mM sucrose, 1 mM EDTA and 1 mM PMSF; supernatants were collected by centrifugation at 20,000 × g (4 °C for 30 min). Protein content was calculated using the method of Bradford with bovine serum albumin (BSA) as a standard, and equal loading was confirmed electrophoretically by diluting samples directly into sample buffer up to a volume of 20 μL [44].

SOD activity was measured according to the method described by McCord and Fridovich [45]. It is expressed as units (U), where 1 U is the amount of sample required to cause 50% inhibition of the rate of reduction of cytochrome c by the superoxide anion generated by the xanthine/hypoxanthine system. The reaction mixture contained 43 mM KH_2PO_4/K_2HPO_4 (pH 7.8), 10 mM cytochrome C, 0.1 mM EDTA, 50 mM hypoxanthine, 1.8 mUm/L xanthine oxidase and 100 mL of the cytosolic fraction from the gill homogenates, in a final volume of 3 mL. The SOD activity is expressed in mol/min/mg of total protein. CAT activity was measured according to Claiborne [46] in which the decrease in hydrogen peroxide (H_2O_2) absorbance at 240 nm is measured. CAT activity is expressed in mol/min/mg of total protein, using a molar extinction coefficient of 40 $M^{-1}\,cm^{-1}$.

Protein thiols present in the supernatant were labeled by adding iodoacetamidofluorescein (IAF) in DMSO to a final concentration of 800 μM and incubating at room temperature for 2 h in the dark. IAF reacts specifically with reduced thiols (–SH) but not with oxidized variants such as sulfenic acid (–SOH) or disulfides (–S–S–) which might be expected to form via oxidative stress [47].

Proteins were then resolved using one-dimensional electrophoresis (1DE) in 12% polyacrylamide gels [48]. Samples (120 μg proteins) were diluted in buffer lacking β- mercaptoethanol, to avoid reduction of disulfide bridges. Gels were scanned in a Typhoon 9400 scanner (GE Healthcare, UK; excitation, 490–495 nm; emission, 515–520 nm) and were subsequently stained with Coomassie G250. Equal amounts of protein (50 μg per well) were loaded in 12 wells and repeated at least three times. For each gel, bands detected by the Typhoon 9400 scanner were subsequently analyzed by Quantity One image analysis software (Bio-Rad, Hercules, CA USA) measuring the total intensity for each lane, quantified as arbitrary units (A.U.). 1DE gels stained with Coomassie blue G250 were scanned in a GS-800 calibrated densitometer and total optical density of each lane measured by Quantity One image analysis software. Total optical densities for each lane were normalized with those from coomassie staining for the same gel track.

One-way ANOVA was used to test for overall differences between measured biomarker activities in each tank and the Tukey HSD test allowed pairwise comparisons between experimental conditions ($p < 0.05$). The means and standard errors (mean ± SEM) were calculated. Quantitative differences in 1DE gel spots for gill from treated animals were compared with controls using Student's t test.

3 Results and discussion

3.1 Structural, morphological and optical characterizations

The crystalline phase of the as-prepared powder was determined by XRD. Figure 1 shows the XRD spectrum of the deposition product, where three diffraction peaks at $2\theta = 28.56°, 47.52°, 56.29°$, respectively, are found to match well to the (111), (220) and (311) diffraction peaks of sphaleritic ZnS (JCPDS No. 05-0566). This suggests that the product is pure face-centered cubic (FCC) ZnS (space group F-43m, lattice constant $a = 5414(5)$). The broadness of the peaks is due to the small size of the crystals. No diffraction peaks from impurities were detected in the sample. The XRD result

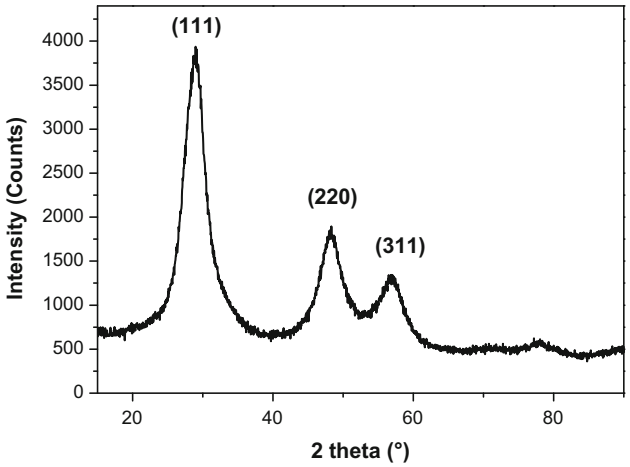

Fig. 1 X-ray diffraction pattern of the ZnS nanoparticles

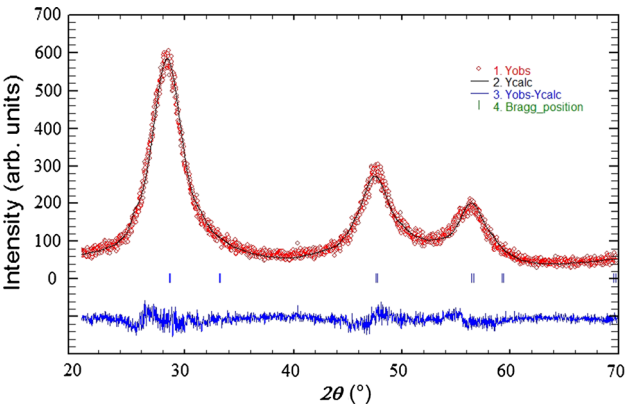

Fig. 2 Profile refinement powder diffractogram of ZnS nanoparticles

indicated that the synthesized ZnS nanoparticles have a good crystallinity. The average size of the ZnS crystallites, estimated from the full-width at half-maximum (FWHM) of the diffraction peak of ZnS (111), (220) and (311) plane, is about 4–5 nm. The lattice parameters of the samples were refined by the Rietveld method [49] from the XRD diffractogram (recorded for 12 h) using the program FULLPROF [50] (Fig. 2). The so-obtained lattice parameters of ZnS NPs were found to be $a = 5.4001$Å. This decrease compared to the bulk material can be attributed to the nanoscale effect [29].

The morphology of pure ZnS nanoparticles was determined by transmission electron microscopy. The TEM images in Fig. 3a, b show that ZnS NPs with a quasi-spherical shape are formed. The size of the prepared ZnS particles is about 5 nm, which is in good agreement with calculated results from XRD patterns. The high-resolution TEM (HRTEM) image in Fig. 3c shows well-defined ZnS crystal planes, thus corroborating the crystalline structure of the formed particles. Lattice fringes can be clearly distinguished for a single ZnS nanocrystals (Fig. 3d) as 0.31-nm interplane spacing of the (111) plane of ZnS in the cubic blende structure [51], in agreement with the XRD result, and the growth direction of the nanocrystals is [111]. Analysis by energy spectroscopy (EDAX) shows that the sample has only peaks of zinc and sulfur, thus confirming the high-purity ZnS nanoparticles (Fig. 4).

Further analysis was conducted by FTIR spectroscopy to examine the chemical compositions of the outer surface of ZnS nanoparticles. Figure 5 presents the spectrum of a representative case, ZnS nanoparticles functionalized with 1,3-propanediol solvent molecules. Indeed, it can be seen that despite the successive washes of the powder with absolute ethanol, traces of solvent still exist, which is confirmed by the presence of a broad and intense band at around 3340 cm^{-1} assigned to the vibrations of valence of OH group of 1.3-propanediol, the relative bands of the two vibrations of valences of the C-H groups at about 2970–2860 cm^{-1} and the valence band located to 1073 cm^{-1}, which is due to the vibrations of the valence bands of the polyol's CO group. It also distinguishes the presence of a band around 1600 and 1400 cm^{-1} assigned to the valence vibrations of the acetate [52]; the vibration of the ZnS bond is confirmed by the presence of the band located around 662 cm^{-1} [53].

The photoluminescence (PL) emission spectrum of pure ZnS nanoparticles with excitation wavelength of 266 nm at room temperature is shown in Fig. 6. In PL process, an electron from the ZnS valence band is excited to conduction band and photo-excited electron decay by a recombination process to defects states. The PL emission of ZnS exhibits one narrow band at 422 nm, which is typical luminescence of undoped ZnS, resulting from the transition of electrons from shallow states near the conduction band to sulfur vacancies present near the valence band [54]. This peak occurs because of the self-trapping hole centers in ZnS [55,56]. The optical absorption spectrum of the powder obtained (Fig. 7a) showed the presence of a band situated around 266 nm characteristic of the formation of ZnS nanoparticles. The treatment of this spectrum by the Tauc method [57] allows determining the energy gap (Eg) to 4.4 eV (Fig. 7b). This value is greater than the solid mass of ZnS (3.6 eV). This result shows clearly a quantum confinement effect in relation to the sheer size of the nanoparticles.

3.2 Electrical properties

The impedance spectroscopy technique is used to analyze the electrical response or transport properties of the materials in a large range of frequencies. It enables us to evaluate and separate the contributions of electrical properties in the electrical parameters in the wide frequency range due the grains, grain boundaries and electrode/sample interface in a polycrystalline materials. The variation of real part of impedance (Z') of ZnS nanoparticles as a function of frequency (10–

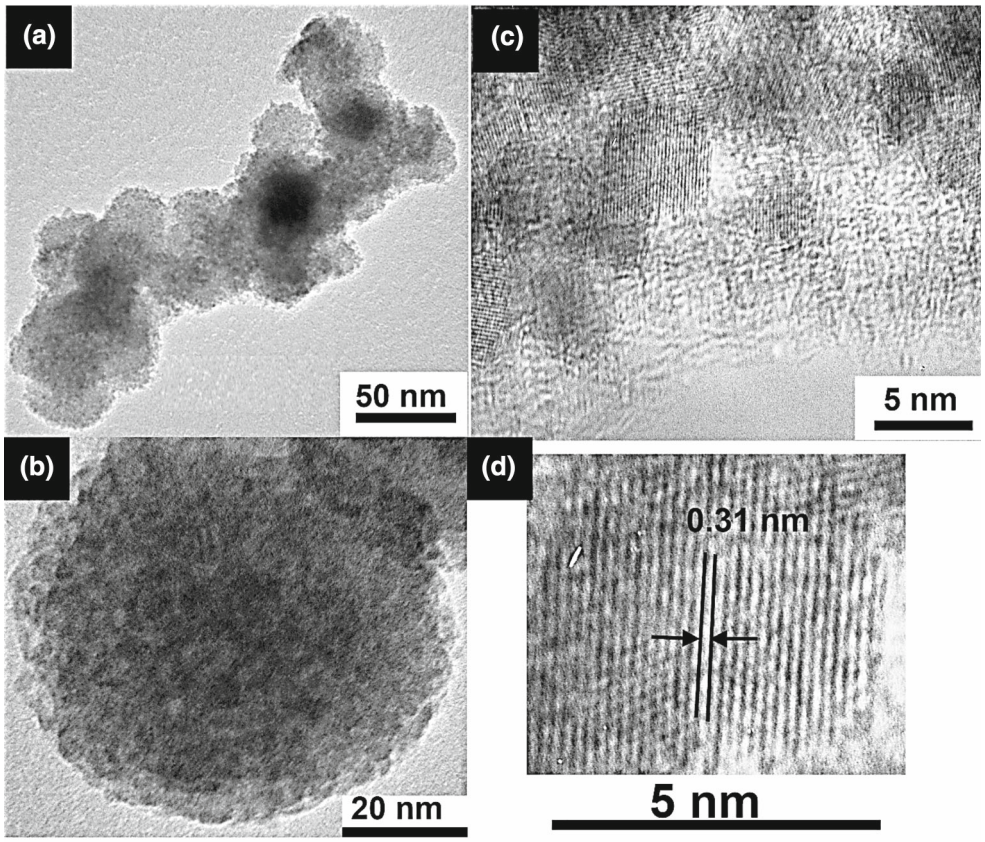

Fig. 3 **a**, **b** TEM images and **c**, **d** HRTEM images of ZnS nanoparticles

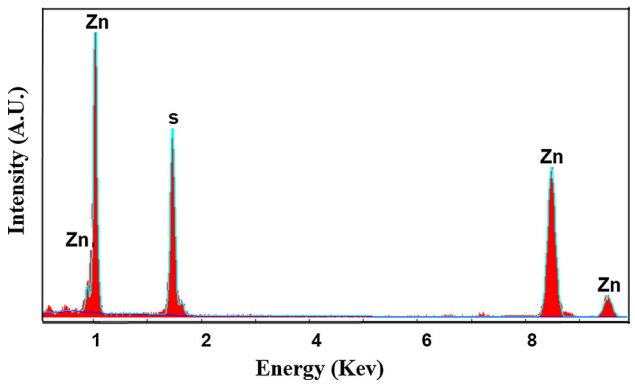

Fig. 4 EDAX spectrum of ZnS nanoparticles

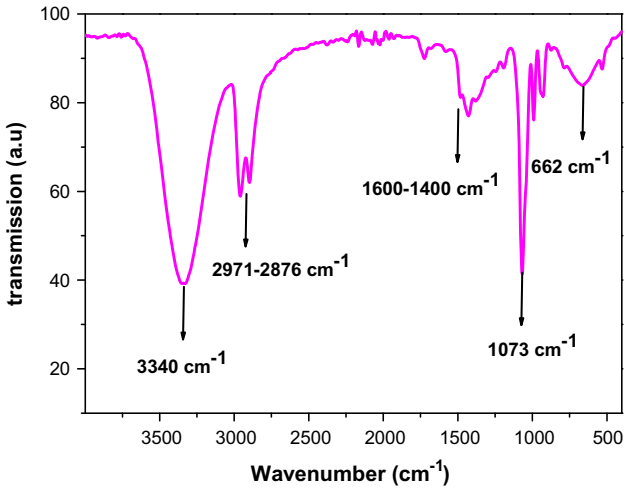

Fig. 5 FTIR spectra of ZnS nanoparticles

10^7Hz) at different temperatures is shown in Fig. 8. The value of Z' decreases with the rise in both frequency and temperature. Therefore, the conducting property of the material increases with the rise of temperature and frequency. At high frequency, Z' values coincide with each other at the all temperatures suggesting the release of space charge [58].

Figure 9 shows the variation of imaginary part of impedance (Z'') with frequency at different temperatures. It can be seen from the graphs that the value of Z'' decreases with increase in temperatures. The decrease in impedance with temperature improves dielectric properties. In these graphs, two peaks appear indicating the presence of at least two dielectric relaxation processes in ZnS nanoparticles. The relaxation processes involved are due to bulk and interface effect. For temperatures lower than 125 °C, the imaginary

part of the impedance (Z'') shows a first peak of relaxation (Fig. 9a), which moves toward higher frequencies when temperature increases. The presence of a single peak in this temperature ranges (lower than 125 °C) for ZnS nanoparticles is in agreement with that found by Hassan Ali et al. [59]. Above 125 °C, the variation of imaginary part of the impedance (Z'') with frequency is shown in Fig. 2b. Z'' value increases initially, reaches the maximum value at particular frequency and then decreases continuously with increasing frequency. With increase in temperature, another peak enters through high-frequency window. This suggests the coexistence of tow relaxation effects which can be attributed to grain and grains boundary responses. The maximum values of Z'' shift to high-frequency side with increasing temperature, which corresponds to plateau relaxation observed earlier in real impedance spectra.

Figure 10 shows the temperature dependence of complex impedance spectra (Nyquist plot) of ZnS nanoparticles. The effect of temperature on impedance and related parameters of materials becomes clearly visible with rise in temperature. On increasing temperature, the slope of the lines decreases, and hence, they bend toward Z'-axis by which semicircle could be formed. At temperature up to 125 °C, the absence of second arc in ZnS nanoparticles confirmed that the polarization mechanism corresponds to the bulk effect arising in semiconductive grains. At higher temperatures (>125 °C), it was possible to trace two semicircles. The appearance of two semicircles suggests the presence of both bulk (grain) (at the high-frequency region) as well as grain boundary effect (at the low-frequency region) in the studied sample.

The bulk conductivity (σ) value has been calculated using the formula, $\sigma = L/R_b A$ S m^{-1} where R_b is bulk resistance of the sample, L is the thickness of the pellet and A is the effective area. The AC conductivity is a important parameter, used to characterize the dielectric properties of materials. Measurement of AC conductivity of semiconductors has been extensively used to understand the transport mechanism in these materials. The AC conductivity (σ_{AC}) is calculated by using the relation, $\sigma = L/R_b A$ S m^{-1} where

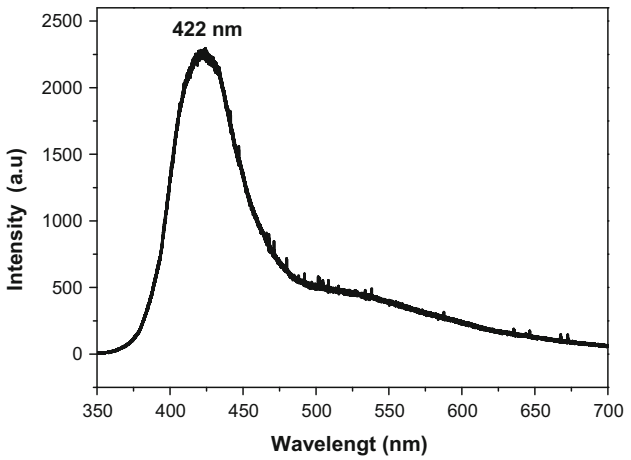

Fig. 6 Photoluminescence (PL) of ZnS nanoparticles

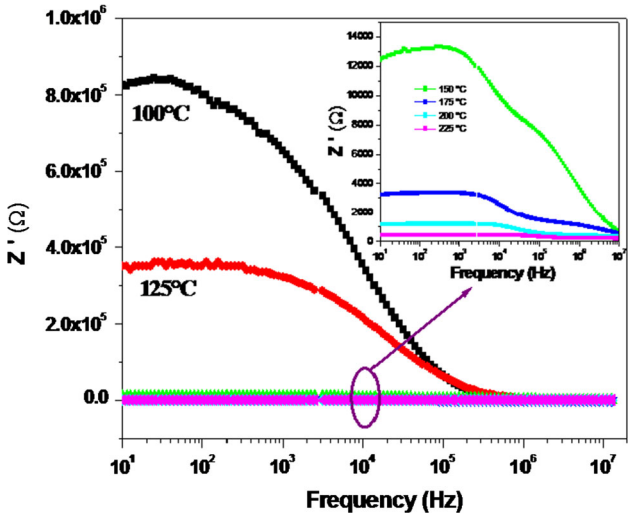

Fig. 8 Frequency dependence of Z' for ZnS nanoparticles at different temperatures between 100 and 225 °C

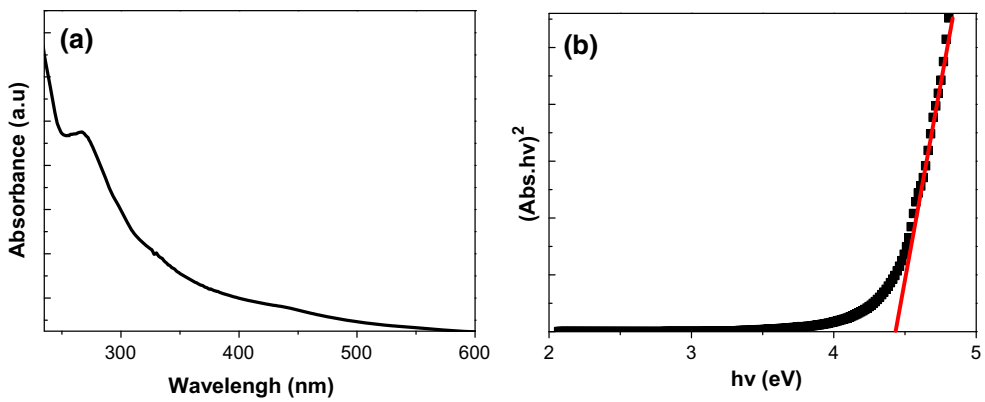

Fig. 7 UV (**a**) and gap energy (**b**) spectra of ZnS nanoparticles

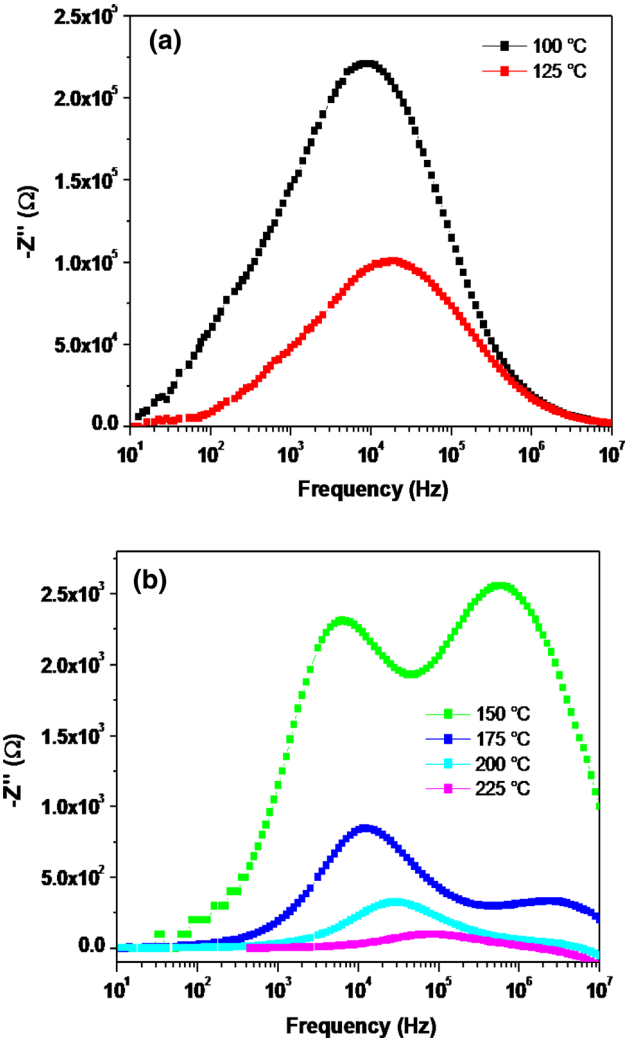

Fig. 9 Variation of imaginary part of impedance with frequency at different temperatures of ZnS nanoparticles

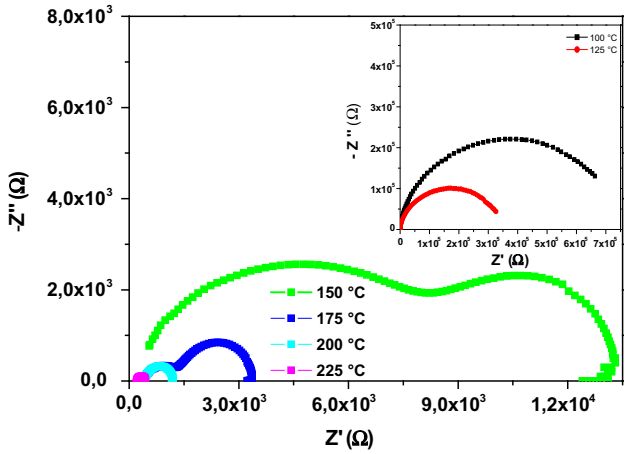

Fig. 10 Complex impedance plot at different temperatures of ZnS nanoparticles

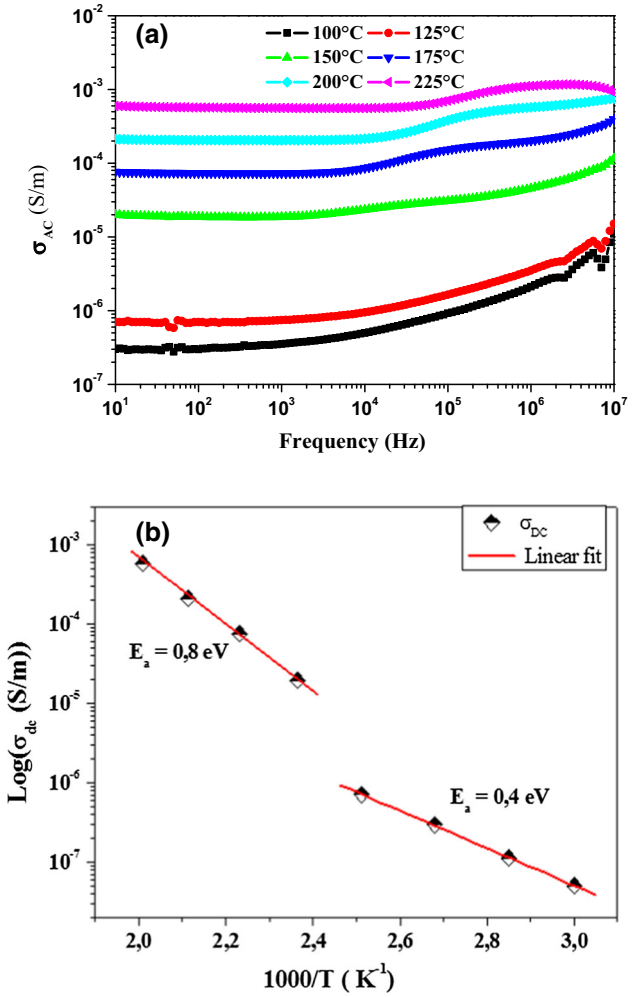

Fig. 11 Frequency variation of AC conductivity (σ_{ac}) at different temperatures and variation of DC conductivity (σ_{dc}) of ZnS with inverse of temperature

R_b is bulk resistance of the sample, L is the thickness of the pellet and A is the effective area. Figure 11a shows the frequency dependence of AC conductivity (σ_{ac}) at different temperatures. It shows that, at low frequency, the conductivity is almost frequency independent. But at high frequency, the conductivity depends on frequency. AC conductivity can be described by Jonscher's power law, i.e [60],

$$\sigma_{ac} = \sigma_{dc} + A\omega^n$$

where σ_{ac} is the AC conductivity, ω is the angular frequency, σ_{dc} is the DC bulk conductivity, A is a pre-exponential constant, and n is the power-law exponent. At temperatures lower than 125 °C, low-frequency plateau and high-frequency dispersion of conductivity appear to be observed. Above 125 °C, the conductivity shows a significant increase with temperature, we also observe a significant change in the conductivity pattern. In this temperature range, a broader plateau region is

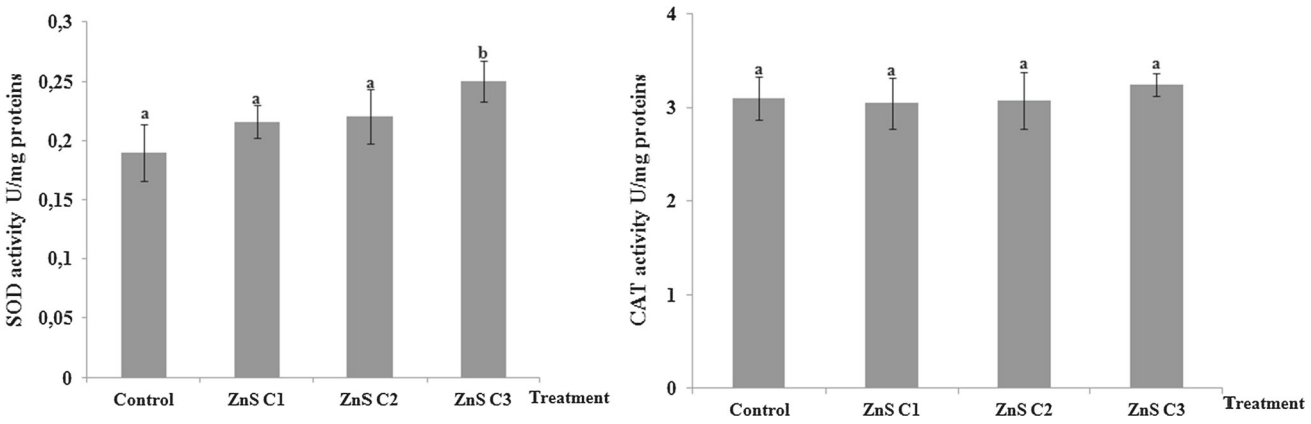

Fig. 12 Superoxide dismutase and catalase activities in gill of untreated (C, control) and treated mussels for short term to ZnS C1 = 0.1 mg/L, ZnS C2 = 1 mg/L and ZnS C3 = 10 mg/L. Significant differences are indicated by *different letters* ($p < 0.05$) (HSD Tukey)

observed in the low-frequency region and a dispersive behavior of conductivity spectrum appears in the high-frequency region irrespective of temperature. The increasing trend of σ_{ac} with rise in frequency may be attributed to the disordering of cations between neighboring sites and presence of space charge [61]. The rise in the value of conductivity with temperature indicates that the electrical conduction in the material is a thermally activated process. Figure 11b shows the variation of DC conductivity (σ_{dc}) with inverse of temperature. The nature of conductivity variation (linear dependence of σ_{dc} with 10^3 T^{-1}) indicates an increase in conductivity with rise in temperature with a typical Arrhenius-type behavior. This suggests that the electrical conduction in the material is a thermally activated process which is governed by the relation:

$$\sigma_{dc} = \sigma_0 \exp\left(\frac{-E_\sigma}{KT}\right),$$

where σ_{dc} is the DC conductivity, σ_o is the pre-exponential factor, T is the temperature in K, E_σ is the DC conductivity activation energy and k is the Boltzmann constant. Fitting of these data to Arrhenius equation yields the activation energy Ea as 0.4 and 0.8 eV for temperatures lower and higher than 125 °C, respectively.

3.3 Ecotoxicological risk

In this study, isolated gills from mussels were used to study the activities of two enzymes, SOD and CAT, measured in response to ZnS exposure (Fig. 12). When comparing to control, no significant difference was observed in SOD activity after exposure to 0.1 and 1 mg/L of ZnS. In contrast, significant difference ($p < 0.05$) was detected at high concentration. SOD is an antioxidant enzyme catalyzing the dismutation of two superoxide radicals to hydrogen peroxide and oxygen. SOD activity increased in gill at high amount of ZnS, and this may be due to increase in superoxide anion radical, which is directly neutralized by SOD and converted to hydrogen peroxide. Our study indicates that ZnS NP-induced SOD might occur in the treatment groups at an exposure concentration of ≥1 mg/L. This result is in agreement with [62] reported that exposure to 1.0 mg/L of $nTiO_2$ significantly increased superoxide dismutase activity in *Haliotis diversicolor supertexta*.

CAT is involved in the hydrolysis of H_2O_2 and was one of the first enzymes proposed as an effective biomarker for oxidative stress. In the present study, no significant difference was observed between CAT activity in treated groups and CAT activity in control groups even at high concentration (Fig. 12). This result suggests that the presence of ZnS in the environment even at 10 mg/L cannot induce oxidative stress in *M. galloprovincialis*. Additionally, these observations can be explained by the modest level of oxidative stress caused by ZnS at these concentrations. Previous studies were observed similar enzymatic profile in *M. galloprovincialis* and oyster exposed to fullerene nanoparticles [63,64].

Protein thiols play numerous roles in biology including in antioxidant defense and absorption of ROS resulting in their oxidation to derivatives. The roles of proteins in signal transduction pathways depend strongly on the redox properties, which occur both in proteins and in low molecular mass thiols [65]. Thiols react with oxidizing species and thus contribute to antioxidant defense [66,67]. NPs have strong affinity for protein thiol groups (Krpetic et al., 2009; Aubin-Tam et al., 2009). In the present study, 1D gel results showed no statistical difference for gill after ZnS treatment in terms of thiols density even at high concentrations ZnS C3 = 10 mg/l (Fig. 13). This result confirms those obtained in enzymatic assay and supports that ZnS does not necessarily cause generation of ROS as well as oxidation of thiols groups at an exposure concentration of ≤10 mg/L .

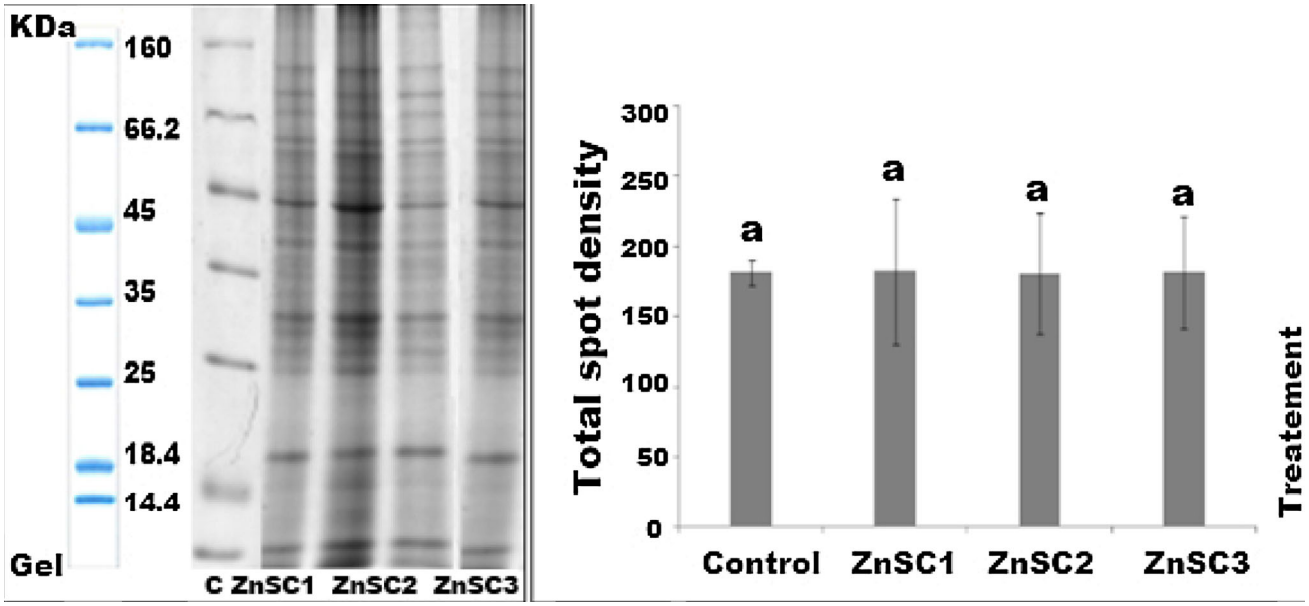

Fig. 13 1DE gel results for protein thiols in gill of mussels exposed for short term to ZnS C1 = 0.1 mg/L, ZnS C2 = 1 mg/L and ZnS C3 = 10 mg/L. Significant differences are indicated by *different letters* ($p < 0.05$) (Student's t test)

4 Conclusion

ZnS nanocrystals with a mean diameter of 5 nm were synthesized for the first time by means of a facile polyol-mediated route using 1,3-propanediol as a solvent and zinc acetate $Zn(CH3COO)_2$ as a precursor. The polyol solvent plays the roles of the stabilizer and the template. The facile and low-cost synthesis method reported in this work may open the way to new applications for very small ZnS nanoparticles. The electrical property study of the sample was also performed, the results show that the variation of AC conductivity (σ_{ac}) with frequency obeys to Jonscher power law. The DC conductivity (σ_{dc}) shows typical Arrhenius behavior when observed as a function of temperature. However, we can deduce according to the presented measurements that the electrical properties of ZnS NPS reveal the existence of bulk and grain boundary phases. On the other hand, we have also studied the ZnS effects in the sentinel, *M. galloprovincialis* to underline such potential environmental risk. No effects were observed in SOD and CAT activities or on the levels of protein thiols under the conditions used. ZnS is not therefore a pro-oxidant at an exposure concentration of $\leq$10 mg/L and has no potential environmental risk at this level. Further studies based on longer exposure times and/or high concentrations are necessary to explore the effects of these nanoparticles further and to better support the use of this nonmaterial on various applications.

Acknowledgements Anis Fkiri gratefully acknowledges the support of the Ministry of Higher Education and Scientific Research of Tunisia.

References

1. Bao H, Hao N, Yang Y, Zhao D (2010) Biosynthesis of biocompatible cadmium telluride quantum dots using yeast cells. Nano Res 3:481–489
2. Tang ZY, Wang Y, Shanbhag S, Kotov NA (2006) Spontaneous CdTe → Alloy → CdS transition of stabilizer-depleted cdte nanoparticles induced by EDTA. J Am Chem Soc 128:7036–7042
3. Cao YC, Wang JH (2004) One-pot synthesis of high-quality zinc-blende CdS nanocrystals. J Am Chem Soc 126:14336–14337
4. Zhang J, Wu Y, Zhu J, Huang S, Zhang D, Yin Q (2010) Synthesis and optical properties of self-assembled flower-like CdS architectures by mixed solvothermal process. Cent Eur J Chem 85:1027–1033
5. Swain B, Hong MH, Kang L, Kim BS, Kim N-H, Lee CG (2017) Optimization of CdSe nanocrystals synthesis with a microfluidic reactor and development of combinatorial synthesis process for industrial production. J Chem Eng 308:311–321
6. Brahim BB, Naim BHM, Poggi M, Rafik BC, Mohammed H, Hafedh BO, Negrerie M (2017) Interaction of l-cysteine functionalized CdSe quantum dots with metallic cations and selective binding of cobalt in water probed by fluorescence. Sen Actuators B Chem B243:489–499
7. Tang Z, Zhang Z, Wang Y, Glotzer SC, Kotov NA (2006) Self-assembly of CdTe nanocrystals into free-floating sheets. Science 314:274–278
8. Chieng BW, Loo YY (2012) Synthesis of ZnO nanoparticles by modified polyol method. J Mater Lett 73:78–82
9. Trenque I, Mornet S, Duguet E, Gaudon M (2013) New insights into crystallite size and cell parameters correlation for ZnO nanoparticles obtained from polyol-mediated synthesis. Inorg Chem 52:12811–12817
10. Wang K, Xub X, Ma L, Wang A, Wang R, Luo J, Wen S (2017) Studies on triboluminescence emission characteristics of various kinds of bulk ZnS crystals. J Lumin 186:307–311

11. Mullamuri B, Bhagavathula SD, Kasturi Krishna CSB, Reddy V (2017) Facile synthesis of bovine serum albumin conjugated low-dimensional ZnS nanocrystals. Int J Biol Macromol 101:729–735
12. Mirzadeh S, Darezereshki E, Bakhtiari F, Fazaelipoor MH, Hosseini MR (2013) Characterization of zinc sulfide (ZnS) nanoparticles biosynthesized by *Fusarium oxysporum*. Mater Sci Semicond Proc 16:374–378
13. Yue L, Qi S, Wang J, Cai J, Xin B (2016) Controllable biosynthesis and characterization of α-ZnS and β-ZnS quantum dots: comparing their optical properties. Mater Sci Semicond Proc 56:115–118
14. Geng BY, Liu XW, Ma JZ, Du QB, Zhang LD (2007) Size-dependent optical and electrochemical band gaps of ZnS nanorods fabricated through single molecule precursor route. Appl Phys Lett 90:183106–183108
15. Yu JH, Joo J, Park HM, Baik S, Kim YW, Kim SC, Hyeon T (2005) Synthesis of quantum-sized cubic ZnS nanorods by the oriented attachment mechanism. J Am Chem Soc 127:5662–5670
16. Zhang YJ, Xu HR, Wang QB (2010) Ultrathin single crystal ZnS nanowires. Chem Commun 46:8941–8943
17. Deng ZT, Yan H, Liu Y (2010) Controlled colloidal growth of ultrathin single-crystal ZnS nanowires with magic-size diameter. Angew Chem Int Ed 49:8695–8698
18. Xu JF, Ji W, Lin JY, Tang SH, Du YW (1998) Preparation of ZnS nanoparticles by ultrasonic radiation method. Appl Phys A 66:639–641
19. Jiang Z, Sun H, Qin Z, Jiao X, Chen D (2012) Synthesis of novel ZnS nanocages utilizing ZIF-8 polyhedral template. Chem Commun 48:3620–3622
20. Wang Z, Daemen LL, Zhao Y, Zha CS, Downs RT, Wang X, Wang ZL, Hemley RJ (2005) Morphology-tuned wurtzite-type ZnS nanobelts. Nat Mater 4:922–927
21. Li J, Zhang Q, An L, Qin L, Liu J (2008) Large-scale growth of millimeter-long single-crystalline ZnS nanobelts. J Solid State Chem 181:3116–3120
22. Zhang Y, Peng Q, Li YD (2004) Synthesis and characterization of monodisperse ZnS nanospheres. Chem Lett 33:1320–1321
23. Star V, Etsell TH, Pierre AC, Mikula RJ (1997) Sol-gel processing of ZnS. Mater Lett 31:35–38
24. Jiang C, Zhang W, Zou G, Yu W, Qian Y (2007) Hydrothermal synthesis and characterization of ZnS microspheres and hollow nanospheres. Mater Chem Phys 103:24–27
25. Yao WT, Yu SH, Wu QS (2007) From mesostructured wurtzite ZnS-nanowire/amine nanocomposites to ZnS nanowires exhibiting quantum size effects: a mild-solution chemistry approach. Adv Funct Mater 17:623–631
26. Fang XH, Bando YH, Shen G, Golberg D (2007) Shape- and Size-controlled Growth of ZnS Nanostructures. J Phys Chem C 111:8469–8474
27. Liao XH, Zhu JJ, Chen HY (2001) Microwave synthesis of nanocrystalline metal sulfides in formaldehyde solution. Mater Sci Eng B 85:85–89
28. Wilhelmy DM, Matijevic E (1984) Preparation and properties of monodispersed spherical-colloidal particles of zinc sulphide. J Chem Soc 80:563–570
29. Mezni A, Kouki F, Romdhane S, Fonrose BW, Joulie S, Mlayah A, Smiri LS (2012) Facile synthesis of ZnO nanocrystals in polyol. J Mater Lett 86:153–156
30. Feldman C (2005) Polyol-mediated synthesis of nanoscale functional materials. Solide State Sci 7:868–873
31. Chong B, Liqing P, Zhengang G, Yuelei Z, Miaofeng H, Xin J, Xiao JQ (2010) Facile fabrication of wurtzite ZnS hollow nanospheres using polystyrene spheres as templates. Mater Lett 64:1681–1683
32. Girardello F, Leite CC, Branco CS, Roesch-Ely M, Fernandes AN, Salvador M, Henriques JAP (2016) Antioxidant defences and haemocyte internalization in *Limnoperna fortunei* exposed to TiO2 nanoparticles. J Aquat Toxicol 176:190–196
33. Bebianno MJ, Serafim MA (2003) Variation of metal and metallothionein concentrations in a natural population of *Ruditapes decussates*. Arch Environ Contam Toxicol 44:53–66
34. Bodin N, Burgeot T, Stanisiere JY, Bocquene G, Menard D, Minier C, Boutet I, Amat A, Cherel Y, Budzinski (2004) Seasonal variations of a battery of biomarkers and physiological indices for the mussel *Mytilus galloprovincialis* transplanted into the northwest Mediterranean Sea. Comp Biochem Physiol 138:411–427
35. Lionetto MG, Giordano R, Caricato R, Pascariello MF, Marinosci L, Schettino T (2001) Biomonitoring of heavy metal contamination along the Salerno coast (Italy) by metallothionein evaluation in *Mytilus galloprovincialis* and *Mullus barbatus*. Aquat Conserv Mar Freshw Ecosyst 11:305–310
36. Goldberg ED, Bertine KK (2000) Beyond the mussel watch—new directions for monitoring marine pollution. Sci Total Environ 247:165–174
37. Mrdaković M, Ilijin L, Vlahović M, Matić D, Gavrilović A, Mrkonja A, Mataruga Perić V (2016) Acetylcholinesterase (AChE) and heat shock proteins (Hsp70) of gypsy moth (*Lymantria dispar* L.) larvae in response to long-term fluoranthene exposure. Chemosphere 159:565–569
38. Dailianis S (2011) Environmental impact of anthropogenic activities: the use of mussels as a reliable tool for monitoring marine pollution. In: McGevin LE (ed) Mussels: anatomy, habitat and environmental impact. Nova Sciences Publishers Inc., New York, pp 43–72
39. Allen JI, Moore MN (2004) Environmental prognostics: is the current use of biomarkers appropriate for environmental risk evaluation. Mar Environ Res 58:227–232
40. Lam PKS, Gray JS (2003) The use of biomarkers in environmental monitoring programmes. Mar Pollut Bull 46:182–186
41. Tedesco S, Jaafar SNT, Coelho AV, Sheehan D (2012) Protein thiols as novel biomarkers in ecotoxicology: a case study of oxidative stress in *Mytilus edulis* sampled near a former industrial site in Cork Harbour, Ireland. JIOMICS 2:39–47
42. Schmidt W, Rainville LC, McEneff G, Sheehan D, Quinn B (2013) A proteomic evaluation of the effects of the pharmaceuticals diclofenac and gemfibrozil on marine mussels (*Mytilus* spp.): evidence for chronic sublethal effects on stress-response proteins. Drug Test Anal 3:210–219
43. Pedriali A, Riva C, Parolini M, Cristoni S, Sheehan D, Binelli A (2013) A redox proteomic investigation of oxidative stress caused by benzoylecgonine in the freshwater bivalve Dreissena polymorpha. Drug Test Anal 5:646–656
44. Bradford MM (1976) A rapid and sensitive method for the quantitation of microgram quantities of protein utilizing the principle of protein-dye binding. Anal Biochem 72:248–254
45. McCord JM, Fridovich I (1969) Superoxide dismutase. An enzymic function for erythrocuprein (hemocuprein). Biol Chem 244:6049–6055
46. Claiborne A (1985) Catalase activity. In: Greenwald RA (ed) CRC handbook of methods for oxygen radical research. CRC Press, Boca Raton, pp 283–284
47. McDonagh B, Sheehan D (2008) Effects of oxidative stress on protein thiols and disulphides in *Mytilus edulis* revealed by proteomics: actin and protein disulphide isomerase are redox targets. Mar Environ Res 66:193–195
48. Laemmli UK (1970) Cleavage of structural proteins during the assembly of the head of bacteriophage T4. Nature 227:680–685
49. Rietveld Hugo MJ (1967) Line profiles of neutron powder-diffraction peaks for structure refinement. J Appl Cryst 22:151–152
50. Rodriguez-Carvajal J (1990) Collected abstract of powder diffraction meeting, Toulouse, p 127
51. Labiadh H, Chaabane T, Piatkowski D, Mackowski S, Lalevée J, Ghanbaja J, Aldeek F, Scgneider R (2013) Aqueous route to

color-tunable Mn-doped ZnS quantum dots. J Mater Chem Phys 140:674–682
52. Basti H, Tahar LBen, Smiri LS, Herbest F, Vaulay M-J, Chau F, Ammar S, Benderbous S (2010) Catechol derivatives-coated Fe_3O_4 and gamma-Fe_2O_3 nanoparticles as potential MRI contrast agents. J Coll Surf Sci 341:248–254
53. Mohagheghpour E, Rabice M, Mortarzadeh F, Tahriri M, Jafarbeglou M, Bizari D, Eslami H (2009) Controllable synthesis, characterization and optical properties of ZnS: Mn nanoparticles as a novel biosensor. Mater Sci Eng C 29:1842–1848
54. Suyver JF, Wuister SE, Kelly JJ, Meijerink A (2001) Synthesis and photoluminescence of nanocrystalline ZnS:$Mn2^{+}$. Nano Lett 1:429–433
55. Wageh S, Ling ZS, Rong XX (2003) Growth and optical properties of colloidal ZnS nanoparticles. J Cryst Growth 255:332–337
56. Bao H, Hao N, Yang Y, Zhao D (2010) Biosynthesis of biocompatible cadmium telluride quantum dots using yeast cells. Nano Res 3:481–489
57. Costa MM, Pires JGFM, Terezo AJ, Graca MPF, Sombra ASB (2011) Impedance and modulus studies of magnetic ceramic oxide $Ba_2Co_2Fe_{12}O_{22}(Co_2Y)$ doped with Bi_2O_3. J Appl Phys 110:034107(1)–034107(7)
58. Ali H, Karim S, Rafiq MA, Maaz K, Rahman A, Nisar A, Ahmad M (2014) Electrical conduction mechanism in ZnS nanoparticles. J Alloys Compd 612:64–68
59. Jonscher AK (1977) The 'universal' dielectric response. Nature 267:673–679
60. Nithya VD, Selvan R Kalai (2011) Synthesis, electrical and dielectric properties of $FeVO_4$ nanoparticles. Phys B 406:24–29
61. Zhu X, Zhou J, Cai Z (2011) The toxicity and oxidative stress of TiO_2 nanoparticles in marine abalone (Haliotis diversicolor supertexta). Mar Pollut Bull 63:334–338
62. Ringwood AH, Levi Polyachenko N, Carroll DL (2009) Fullerene exposures with oysters: embryonic, adult, and cellular responses. Environ Sci Technol 43:7136–7141
63. Canesi, Fabbri R, Gallo G, Vallotto D, Marcomini A, Pojana G (2010) Biomarkers in *Mytilus galloprovincialis* exposed to suspensions of selected nanoparticles (Nano carbon black, C60 fullerene, Nano-TiO_2, Nano-SiO_2). Aquat Toxicol 100:168–177
64. Winterbourn CC, Hampton MB (2008) Thiol chemistry and specificity in redox signaling. Free Rad Biol Med 45:549–561
65. Hansen RE, Roth D, Winther JR (2009) Quantifying the global cellular thiol-disulfide status. Proc Natl Acad Sci USA 106:422–427
66. Krpetic Z, Nativo P, Porta F, Brust M (2009) A multidentate peptide for stabilization and facile bioconjugation of gold nanoparticles. Bioconjug Chem 20:619–624
67. Aubin-Tam ME, Hwang W, Hamad-Schifferli K (2009) Site-directed nanoparticle labeling of cytochrome c. Proc Natl Acad Sci USA 106:4095–4100